

Contents lists available at [ScienceDirect](https://www.sciencedirect.com)

# International Journal of Applied Earth Observation and Geoinformation

journal homepage: [www.elsevier.com/locate/jag](http://www.elsevier.com/locate/jag)

## A hybrid machine learning approach to investigate the changing urban thermal environment by dynamic land cover transformation: A case study of Suwon, republic of Korea

Siwoo Lee<sup>a</sup>, Cheolhee Yoo<sup>b,\*</sup>, Jungho Im<sup>a,\*</sup>, Dongjin Cho<sup>a</sup>, Yeonsu Lee<sup>a</sup>, Dukwon Bae<sup>a</sup><sup>a</sup> Department of Urban and Environmental Engineering, Ulsan National Institute of Science and Technology (UNIST), Ulsan, South Korea<sup>b</sup> Department of Land Surveying and Geo-Informatics, The Hong Kong Polytechnic University, Hung Hom, Kowloon, Hong Kong

## ARTICLE INFO

## Keywords:

Urban climate  
Local climate zone  
Land surface temperature  
Urban morphology  
Thermal remote sensing  
Machine learning

## ABSTRACT

Urban thermal environment should be analyzed by considering the dynamic structural changes as cities grow both horizontally and vertically. Local Climate Zone (LCZ) scheme can describe built-up areas in detail, mainly based on density and height; however, the low overall accuracy of LCZ urban classes ( $OA_{urb}$ ) remains a notable limitation that requires improvement. This study proposes a hybrid analytical method considering bidirectional urban expansion and low  $OA_{urb}$ . Temporal LCZ maps were constructed using a convolutional neural network to observe the dynamic urban growth between 2004 and 2021 in Suwon, South Korea. Unlike previous LCZ mapping studies, we utilized the additional information provided by deep learning through softmax-based probability maps. Random forest-based downscaling models were developed by combining various auxiliary variables related to the Land Surface Temperature (LST) to observe the detailed surface energy flux. A filtering method was then employed by eliminating areas where LCZs were identified with a low confidence level using extracted probability maps. Finally, thermal variability was investigated by overlaying the filtered LCZ maps and the corresponding LST. The produced LCZ maps and spatially downscaled LSTs accurately depicted dynamic urban form changes, with the LCZ maps exhibiting an average overall accuracy of approximately 90% and downscaled LSTs showing an average coefficient of determination of  $\sim 0.9$  and a root mean square error of  $0.7\text{ }^{\circ}\text{C}$ . Thermal variability occurring due to structural transitions varied in magnitude depending on the height and density of the buildings, while exhibiting a maximum and minimum value of  $2.8\text{ }^{\circ}\text{C}$  and  $-2.2\text{ }^{\circ}\text{C}$ , respectively. By selecting reliably classified areas, the proposed filtering method produced more rational results than the original non-filtering method, resulting in higher variability from  $-0.4\text{ }^{\circ}\text{C}$  to  $0.6\text{ }^{\circ}\text{C}$ .

### 1. Introduction

Urbanization and population growth have led to the steady replacement of natural land cover with impervious surfaces that absorb large amounts of solar energy and inhibit convective cooling (Oke, 1995; Tomlinson et al., 2011). This causes an imbalance in the energy flow of a city and is associated with a range of localized urban climate issues such as heat waves, air pollution, and Urban Heat Islands (UHIs) (Guo et al., 2022; Wang et al., 2019; Zhao et al., 2020). Densified regions and intensified populations further amplify the overall impact of the observed heat effects (Harlan et al., 2006; Sera et al., 2019). When examining urbanization at the city scale, city growth includes not only impermeable structures that expand horizontally but also urban renewal

that becomes denser and/or extends vertically (Bounoua et al., 2018). Unfortunately, the seemingly inevitable march of urban redevelopment through the construction of high-rise and high-density buildings is currently the only viable option for countering the ever-increasing pressure on limited urban spaces (Reddy, 1996). Therefore, a study of the intra-urban transition is needed to fully understand the urban thermal environment as shaped by the urban configuration.

Studying the atypical and dynamic evolution of urban morphology through urban growth can help maintain sustainable urban development and reduce problems associated with urban expansion (Bhatta, 2009). Previous studies have depicted or obtained land-cover maps to monitor and analyze urban thermal environments over time (Alqurashi et al., 2016; Feyisa et al., 2016; Zhang et al., 2013). However, existing

\* Corresponding authors.

E-mail addresses: [cheolhee.yoo@polyu.edu.hk](mailto:cheolhee.yoo@polyu.edu.hk) (C. Yoo), [ersgis@unist.ac.kr](mailto:ersgis@unist.ac.kr) (J. Im).<https://doi.org/10.1016/j.jag.2023.103408>

Received 1 May 2023; Received in revised form 15 June 2023; Accepted 26 June 2023

Available online 30 June 2023

1569-8432/© 2023 The Authors. Published by Elsevier B.V. This is an open access article under the CC BY-NC-ND license (<http://creativecommons.org/licenses/by-nc-nd/4.0/>).

methodologies have clear limitations for generalization, as researchers are likely to choose non-comparable sources of land use/land cover (LULC) data with different levels of detail (Demuzere et al., 2019; Verburg et al., 2011). In addition, most LULC data have only one category in heterogeneous urban areas (e.g., artificial surface or built-up areas), which makes it challenging to characterize urban climates with multiple surface details (Rwanga et al., 2017; Wang et al., 2019). To address this problem, Stewart and Oke (2012) developed a universally applicable Local Climate Zone (LCZ) classification scheme. The LCZ categorizes urban regions into 17 classes, 10 of which pertain to built-up environments, primarily determined by the density and height of buildings, whereas the remaining seven are related to the natural environment. Leveraging this strength to effectively analyze profound thermal environments, it is now considered a standard for urban landscape classification (Demuzere et al., 2022; Ma et al., 2021).

Many studies have analyzed the urban thermal environment using the LCZ (Chen et al., 2017; Geletić et al., 2019; Kotharkar et al., 2018; Middel et al., 2014; Xia et al., 2022; Yang et al., 2020; Zhao et al., 2022). However, most of these studies have only investigated a single-time LCZ scene that could analyze the spatiotemporal thermal environment of the year under consideration (Bechtel et al., 2019; Zhao et al., 2020). A static, single-time LCZ is ineffective for analyzing the transformation of land cover and the altered intra-urban environment during urbanization. Recently, a multi-temporal LCZ was applied to interpret the multifaceted impact of dynamic land-cover change (Fan et al., 2022; Wang et al., 2019). Despite this innovation, the LCZ classification still has significant shortcomings owing to its low accuracy for urban features. Previous studies have examined historical land cover and thermal environment changes with a relatively low LCZ mapping accuracy (e.g., the Overall Accuracy (OA) is about 60–80%). Notably, the OA of the LCZ urban classes ( $OA_{urb}$ ) was significantly lower than that of the OA for all classes. Thus, the analyses of heat effects in these studies may have high uncertainty owing to many misclassified results. In addition, most previous studies considered only the horizontal development of cities. Other alterations in the urban thermal environment resulting from vertical or density growth within cities have not been sufficiently examined.

The Land Surface Temperature (LST) represents the surface energy flux, making it an important factor in thermal studies (Li et al., 2013; Trigo et al., 2008; Weng and Lu, 2008; Mohammad and Goswami, 2021). Satellite-derived LST data are widely used for spatiotemporal climate analysis because of the spatially continuous information delivered at regular intervals (Cao et al., 2022; Lee et al., 2021; Yoo et al., 2022). Landsat regularly provides valuable LST data with a high spatial resolution (120 m for Landsat 5 and 100 m for Landsat 8 on a 16-day repeat cycle), making it one of the most useful satellites for urban climate researchers (Liu et al., 2011; Cheval et al., 2020). To date, Landsat satellites have been extensively utilized in urban thermal environment analysis to derive land cover maps (Fu and Weng, 2016; Yoo et al., 2019), monitor air temperature (Cho et al., 2020; Ho et al., 2014), assess heat stress (Dugord et al., 2014; Liou et al., 2021), and investigate UHI effects (Lee et al., 2021; Xian et al., 2021). Furthermore, spatial downscaling studies of the LST have been conducted to capture the details of heat fluxes in heterogeneous urban areas (Bonafoni et al., 2016; Zawadzka et al., 2020).

Although previous studies have investigated the relationship between land cover alteration and LST, the strength of its association with dynamic horizontal and vertical urban configuration developments impacted by urban renewal has not yet been adequately examined. However, it is well known that urban regeneration is inevitable as part of the ongoing urbanization process and the associated urban policies designed for efficient land use in cramped city areas. Therefore, it is necessary to analyze the changes in the urban thermal environment and how they are influenced by urbanization-wide morphological transformations. In this study, to analyze the changing thermal environment during urbanization for both horizontal and vertical transformation

processes, we hypothesized that 1) a 30 m spatial resolution of LST finer than 100 m (120 m) of Landsat is necessary to determine the LST variation caused by urban renewal and 2) only regions known to have a low level of LCZ classification uncertainty should be used to examine the heat impact caused by morphological changes between different built-type LCZs. This study proposes the following new strategies to deal with the hypotheses: 1) the retrieval of high spatial resolution LST using artificial intelligence (AI), and 2) a new method for change detection analysis based on a probabilistic deep learning approach.

In this study, Suwon, South Korea was selected as the most suitable city for identifying the thermal impact of rapid urbanization. We sought to answer the following important research questions: (1) Can the newly generated 30 m LST represent the heterogeneous surface energy flux of urban areas? (2) If only areas with high classification accuracy are used for the analysis, is it possible to reliably identify the thermal environment caused by horizontal and vertical urbanization?

Section 2 describes the study area and dataset used in this study. Section 3 elaborates on the specific principles and methodology employed in this research. Section 4 presents the outcomes of the work described in Section 3 as well as LST variation by dynamic structure changes in built-up areas. The last two sections expound on comparing our findings with previous studies, suitability of hypotheses, application of the proposed approach, study limitations, and future directions.

## 2. Study area and data

### 2.1. Study area

The study area was Suwon (37°N, 127°E), which is located approximately 35 km south of Seoul, the capital of South Korea (Fig. 1). Suwon has an area of 121 km<sup>2</sup> and a population of 1.2 million, which is the largest population among the basic local government units in South Korea. Since the 1950s, South Korea has experienced rapid urbanization nationwide (Chen et al., 2020). Suwon is one of the cities experiencing extreme urbanization and population growth (from approximately 0.3 million population in 1980 to 1 million in 2000) (Lee et al., 2007). This has led to extensive land cover changes, with impervious materials expanding both horizontally and vertically. These factors made Suwon an ideal candidate for exploring our hypotheses.

### 2.2. Satellite observation data

Landsat and Shuttle Radar Topography Mission (SRTM) data were used in this study. Landsat 5 Thematic Mapper data consisted of six spectral bands with a spatial resolution of 30 m (band 1–5 and 7) and one thermal band (band 6) at 120 m. Landsat 8 Operational Land Imager/Thermal Infrared Sensor (OLI/TIRS) data consisted of seven spectral bands with a spatial resolution of 30 m (band 1–7) and two thermal bands (band 10–11) at 100 m. Thermal products from both Landsat satellites were resampled to 30 m using a cubic convolutional method. The revisit cycle of both Landsat 5 and 8 was 16 d, and the overpass time of Suwon was approximately 11:00 local time. In this study, considering data quality, availability, and comparability, two scenes per year for each task (LCZ classification and LST spatial downscaling described in Section 3.1–3.2) were used as spectral reflectance (each band) and spectral indices (Normalized Difference Vegetation Index (NDVI) and Normalized Difference Built-up Index (NDBI)) in 2004 (Tables 1, 2).

SRTM was launched by NASA in an attempt to acquire elevation data worldwide in 2000. The SRTM digital elevation model (DEM) was used for extracting topographic (elevation, slope, aspect, and solar radiation) and geometry variables (latitude and longitude) at a resolution of 30 m (Table 2). All of the datasets mentioned above were downloaded from <https://earthexplorer.usgs.gov>.

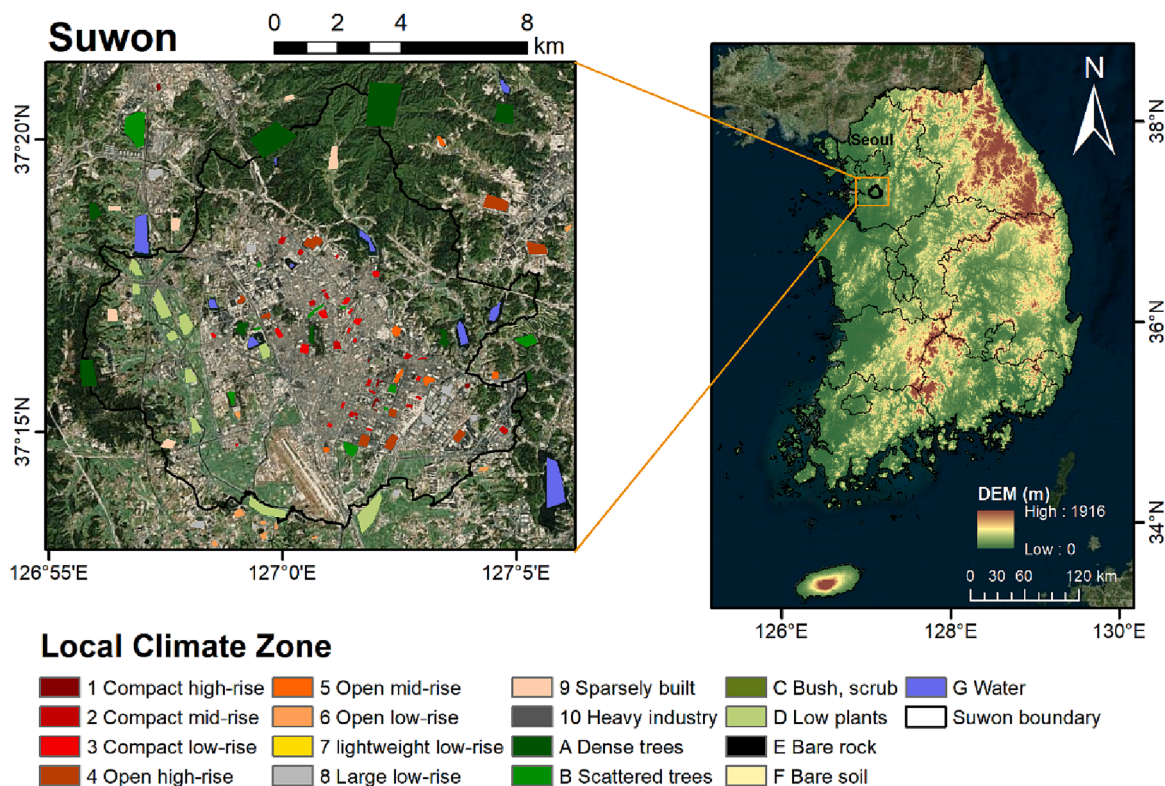


Fig. 1. Study area with the Local Climate Zone (LCZ) reference data. The administrative border is represented by a black line. Shuttle Radar Topography Mission (SRTM) digital elevation model (DEM) with 30 m spatial resolution is used to derive elevation. The background images are from Bing Maps on ArcGIS.

**Table 1**  
Selected Landsat images and sensors for LCZ classification and LST retrieval.

Year	Landsat Scene Identifier	Date Acquired (YY/MM/DD)	Usage
2004	LT51160342004027BJC00	2004/01/27	LCZ classification
	LT51160342004155BJC02	2004/06/03	
2021	LC81160342020343LGN00	2020/12/08	LST retrieval
	LC81160342021153LGN00	2021/06/02	
2004	LT51160342004091BJC00	2004/03/31	LST retrieval
	LT51160342004155BJC02	2004/06/03	
2021	LC81160342021105LGN00	2021/04/15	LST retrieval
	LC81160342021153LGN00	2021/06/02	

### 2.3. Land cover map data

Since 1998, the Ministry of Environment of South Korea has produced nationwide land-cover maps using optical satellites (mainly Landsat and Korean multipurpose satellites) and aerial images. National land-cover maps have been used in various research applications and environmental management. Depending on the resolution, the land cover map was divided into major categories (resolution of 30 m with seven items), middle category (resolution of 5 m with 22 items), and subcategory (resolution of 1 m with 41 items). In this study, land cover data at 30 m resolution with seven items covering the study area were downloaded from <https://egis.me.go.kr/>. Although the study area contained seven land-cover classes in the major categories, some had a small proportion. Therefore, considering the features of cover distribution and proportion in the study area, four classes—urbanized areas (code 100), agricultural areas (code 200), forest areas (code 300), and water bodies (code 700)—were extracted from the major category. Land cover data produced in 2001 and 2019, which were the closest to the study period, were applied as auxiliary variables to generate a fine spatial resolution of LST (Table 2).

**Table 2**  
Data information and their usages.

Source	Variables	Spatial (Temporal) resolution	Usage
Landsat 5	Multispectral band (band 1–5, 7), Normalized Difference Vegetation Index (NDVI), Normalized Difference Built-up Index (NDBI), Thermal band (band 6)	30 m (16 d)	1) LST downscaling
		120 m (16 d)	2) LCZ classification
Landsat 8	Multispectral band (band 1–7), Normalized Difference Vegetation Index (NDVI), Normalized Difference Built-up Index (NDBI), Thermal bands (band 10, 11)	30 m (16 d)	1) LST downscaling
		100 m (16 d)	2) LCZ classification
SRTM	Elevation, Slope, Aspect, Solar radiation, Latitude, Longitude	30 m (–)	LST downscaling
Ministry of Environment Land Cover Map	Percentage of urbanized area, Percentage of forest area, Percentage of agricultural area, Percentage of waterbody	30 m (–)	LST downscaling

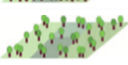
### 2.4. Local climate zones reference data

The remote sensing-based LCZ mapping followed the World Urban Database and Access Portal Tools (WUDAPT) workflow suggested by Bechtel et al. (2015). To ensure the accurate mapping of multitemporal

LCZ scenes, Demuzere et al. (2020) advised the careful selection of reference data for areas that remained unchanged over the long-term study period. Therefore, we generated polygonal LCZ reference data from the representative regions with the same LCZ classes for 2004 and 2021. These reference data were used to develop and evaluate a high-resolution temporal LCZ classification model in accordance with the methodologies suggested by Bechtel et al. (2015) and Demuzere et al. (2020). Eight urban-type LCZs (LCZ1-6, -8, and -9) and four natural-type LCZs (LCZA, B, D, and G) were identified in Suwon (Fig. 1). The reference polygons of each LCZ class were randomly divided into 60% and 40% polygons for model training and evaluation, respectively. Because LCZ1 (compact high-rise) has a relatively small area (i.e., a small sample size) compared to other LCZ classes in Suwon, the LCZ1 pixels, labeled ‘red-star’ as in Yoo et al. (2019), were randomly divided into 60% and 40% for model training and validation, respectively, instead of dividing the polygons (Table 3). Considering the recommendations for the LCZ mapping scale (30–500 m) (Bechtel et al., 2015; Verdonck et al., 2017) and the need to characterize urbanization with a fine spatial resolution (Bounoua et al., 2018), we selected a 30 m scale for LCZ mapping.

**Table 3**

Training and test datasets of each LCZ class for Suwon. The values in the training and test columns indicate the number of polygons and the corresponding pixels at 30 m resolution shown in the parentheses. \* is allocated to the red-star class, which occupies relatively few small areas of the LCZ classes. The LCZ figures in the first column are taken from Stewart and Oke (2012).

LCZ	Suwon	
	Training	Test
 LCZ1 Compact high-rise	9 (146) *	
 LCZ2 Compact midrise	9 (275)	8 (207)
 LCZ3 Compact low-rise	7 (281)	7 (215)
 LCZ4 Open high-rise	5 (706)	4 (527)
 LCZ5 Open midrise	6 (306)	5 (253)
 LCZ6 Open low-rise	5 (160)	5 (121)
 LCZ7 Lightweight low-rise	–	–
 LCZ8 Large low-rise	5 (548)	6 (434)
 LCZ9 Sparsely built	4 (469)	4 (479)
 LCZ10 Heavy industry	–	–
 LCZA Dense trees	6 (2455)	5 (1884)
 LCZB Scattered trees	5 (741)	6 (526)
 LCZC Bush, scrub	–	–
 LCZD Low plants	5 (1156)	5 (930)
 LCZE Bare rock or paved	–	–
 LCZF Bare soil or sand	–	–
 LCZG Water	5 (1030)	5 (991)

### 3. Methodology

The overall flow for exploring the thermal impact of dynamically changing the intra-urban configuration consists of three main parts: 1) LCZ classification, 2) LST downscaling, and 3) thermal variation analysis by LCZ transformation (Fig. 2). In the first part, not only the temporal LCZ maps, but also the deep-learning-based probability maps proposed in this study were extracted. Subsequently, using the kernel-driven approach, the Landsat LST at 100–120 m resolution was downscaled to 30 m resolution in order to observe the surface energy flow for each LCZ type. Finally, after filtering out the LCZs classified with low probability using probability maps, the downscaled LSTs were overlaid to measure the amount of LST change triggered by the LCZ transformation.

#### 3.1. LCZ mapping using convolutional neural Networks

Methods that use Geographic Information Systems (GIS) (Unger et al., 2014) and satellite data-based machine learning (random forest; RF) (Bechtel et al., 2015) techniques have become mainstream for generating LCZs. Later research demonstrated that Convolutional Neural Networks (CNN), an image-based deep learning algorithm, was superior to RF for LCZ classification (Yoo et al., 2019; Rosentreter et al., 2020; Qiu et al., 2020). Thus, the satellite-based CNN approach was adopted to delineate temporal LCZ maps in this work. Unlike other conventional machine learning-based classification models, a CNN was designed to learn the spatial information of an image by exploiting convolutional filters (Kattenborn et al., 2021). Because of their ability to capture spatial patterns, CNN have been frequently employed in classification applications, demonstrating excellent performance (Alhichri et al., 2021; Boulila et al., 2021; Kim et al., 2018; Yoo et al., 2019).

Typically, CNN consist of convolutional, pooled, and fully connected layers. Convolutional layers are instrumental in extracting the features of the input images using moving filters (or kernels). Pooling layers reduce the size (width and height) of the feature map in the process of describing the representative values (i.e., mean or maximum) of the given moving filter but help prevent overfitting. In this study, max pooling, which is commonly used in image categorization, was employed (Guidici et al., 2017; Masolele et al., 2021; Yoo et al., 2019). A fully connected layer converts the lastly extracted two-dimensional feature maps into one-dimensional vector via flattening.

Keras, an open-source software library, was used to implement the CNN. Fig. 3 shows the architectures of the CNN models employed in this study. The optimal structure and hyperparameter tuning are employed using typical heuristic processes. Specifically, the constructed CNN model comprises two large convolutional units with three convolutional layers, two max-pooling layers, and a fully connected layer. All convolutional layers have  $3 \times 3$  kernel sizes, and each side of the input is zero-padded by one pixel during convolution to maintain a constant size of the feature maps. Furthermore, a rectified linear unit (ReLU) with the advantage of efficient computational characteristics was used as the activation function for each convolutional layer. Maximum pooling layers of size  $2 \times 2$  are applied after the third and sixth convolutional layers. A fully connected layer with 256 nodes is placed at the end. To classify the LCZ type, a softmax function was used to assign the output of the fully connected layer with the highest probability to the final class (Equation (1)). To reduce the error function, an adaptive moment estimation (ADAM) optimizer is applied, which is frequently employed in neural networks, particularly in classification problems. Model training with batch sizes of 256 and 1000 epochs was accelerated using a graphics processing unit (GPU) of Nvidia GTX 1080Ti with 11 GB of memory. In this study, unlike most existing LCZ classification studies, a probability map comprising the highest probability of each pixel was also extracted as another output. The probability map was then employed to filter out LCZ pixels with low confidence in our LCZ maps so that they would not be included in the thermal variation analysis by LCZ transformation.

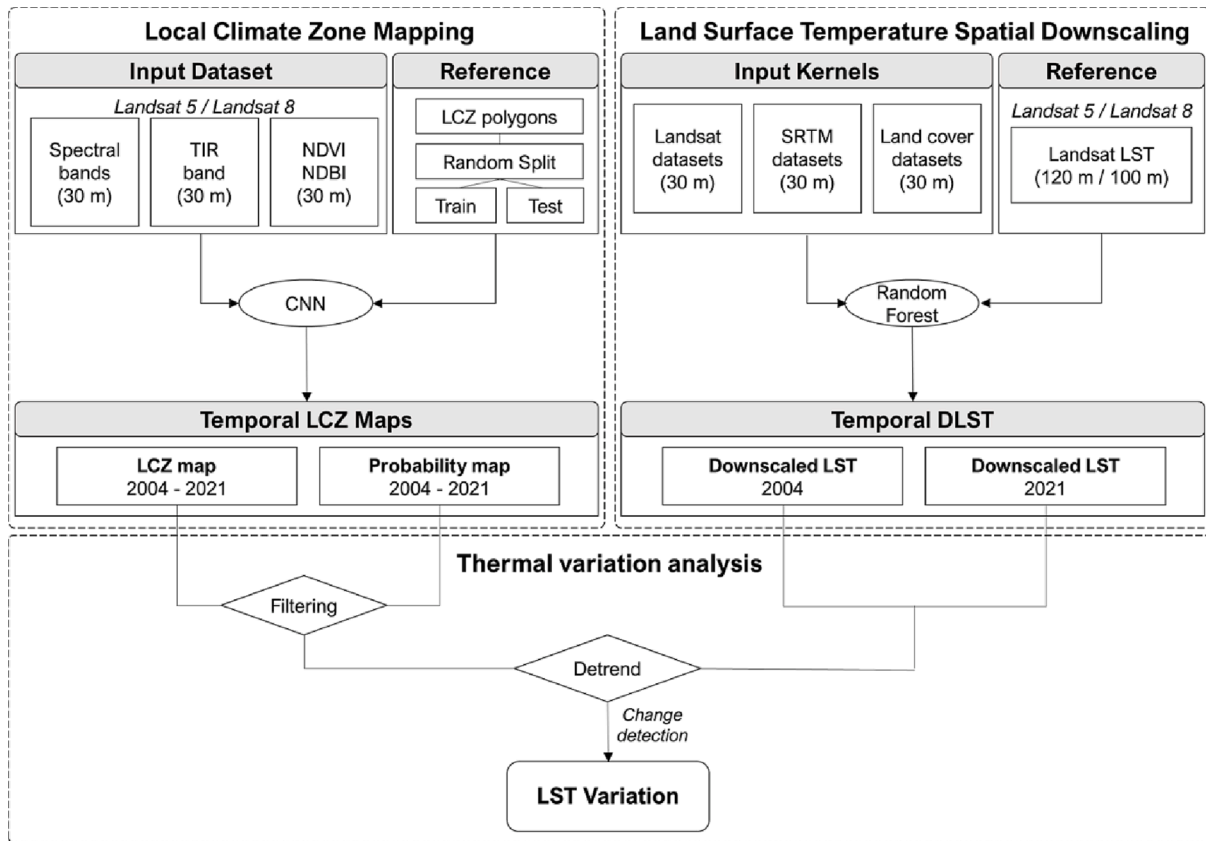


Fig. 2. Illustration of the proposed hybrid AI approach for urban thermal environmental analysis. The procedures are divided into three sections: Local Climate Zone (LCZ) mapping, Land Surface Temperature (LST) downscaling, and thermal variation analysis by LCZ transformation.

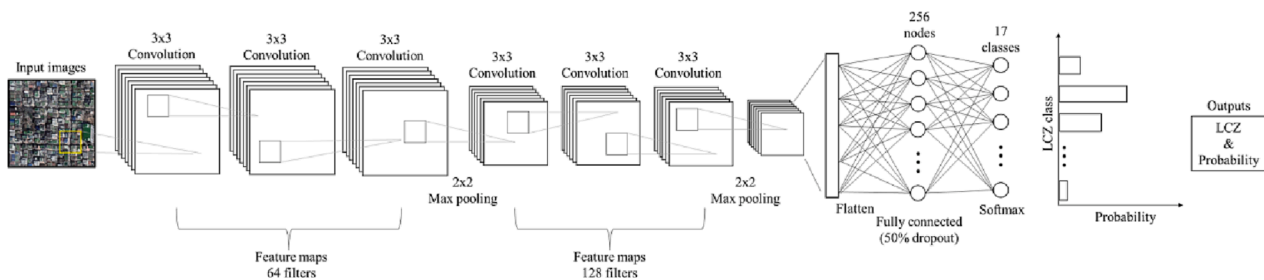


Fig. 3. Architecture of the Convolutional Neural Networks model used in this study.

$$Softmax(y_i) = \frac{e^{y_i}}{\sum_{i=1}^K e^{y_i}} \quad (1)$$

where  $y_i$  is the probability of the output layer of each LCZ class and  $K$  is the total number of LCZ classes in Suwon.

Detailed, high-accuracy LCZ maps are required to investigate the thermal impact of the modified built-type LCZs. Therefore, methods that consider the surrounding area of a focus pixel (Yoo et al., 2019) and the phenology of vegetation (Bechtel et al., 2015) and expand spectral indices as input values (Demuzere et al., 2019) have been used to improve classification accuracy. To consider the surrounding area of a focus pixel, we retrieved  $10 \times 10$  window size features of 30 m resolution Landsat images and fed them into the CNN classifier. Two clear-sky Landsat images obtained during the summer and winter seasons of each year were used to account for vegetation phenology (Table 1). The spectral indices, NDVI and NDBI, were calculated from Landsat satellite spectral band composite data (Equations (2), (3)). We used features created from 18 bands (nine bands for one scene) from Landsat 5 and 22

bands (11 bands for one scene) from Landsat 8 to generate the 2004 and 2021 LCZ maps, respectively (Table 2). An accuracy assessment was conducted using independent validation samples for  $OA_{urb}$ , which is the accuracy of the built-up LCZ types (LCZs 1–10), and  $OA_{nat}$ , which is the accuracy of the natural LCZ types (LCZs A–G).

$$NDVI = \frac{NIR - RED}{NIR + RED} \quad (2)$$

$$NDBI = \frac{SWIR - NIR}{SWIR + NIR} \quad (3)$$

### 3.2. Spatial downscaling of Landsat LST

In urban climate studies that require detailed resolution, an LST resolution finer than 100 m is suitable for approaching typical building widths and blocks (Bechtel et al., 2012). To quantify the rate of change in impervious surfaces and model their effects on the energy cycle, it is crucial to have a high level of detail to detect changes in building type

within a single building block (Bounoua et al., 2018). Considering the demand for fine resolution, the target spatial resolution of the down-scaled LST was determined to be 30 m to observe changes in built-up LCZs and to examine the effects of urban renewal on the thermal environment. To enhance the spatial resolution of LST, statistical down-scaling is often applied using the relationship between multiple highly related input variables, such as surface reflectance, band indexes, and other factors. Among the various downscaling approaches, the kernel-driven method, in which the input variables are called kernels, is considered the most efficient approach for deriving a finer LST in urban areas (Yoo et al., 2020).

RF regression models were implemented to generate a 30 m spatial resolution LST. RF, which comprises multiple decision trees to prevent overfitting and increase accuracy, is a prominent machine learning model for regression and classification (Breiman, 2001). For regression tasks, the combination of multiple decision trees plays a role in decreasing errors owing to the use of bootstrap aggregation or bagging. Owing to its high generalization capability and stable fitting ability in modeling, RF is a preferred machine-learning method for enhancing the spatial resolution of LST (Hutengs and Vohland, 2016; Peng et al., 2021).

Reflectance-based kernels (satellite spectral reflectance data and spectral indices) from Landsat satellites, SRTM DEM-based kernels (topographic and geometric products), and land cover-based kernels from the Ministry of Environment Land Cover map were selected as input kernels to generate a 30 m spatial resolution of LST. All the selected input kernels have been frequently employed in LST down-scaling in heterogeneous urban areas (Bonafoni et al., 2016; Peng et al., 2021; Yoo et al., 2022). Including reflectance indices (i.e., NDVI and NDBI), nine reflectance variables and 11 reflectance-based data were extracted from the Landsat 5 and Landsat 8 satellites, respectively. Four topographic kernels (aspect, elevation, slope, and solar radiation) and two geometric kernels (latitude and longitude) were derived from the SRTM DEM with a 30 m spatial resolution using the Spatial Analyst toolbox in ArcGIS. A total of 19 (nine reflectance-based kernels from Landsat 5, four land-cover-based kernels, and six STRM DEM-based kernels) and 21 kernels (11 reflectance-based kernels from Landsat 8, four land-cover-based kernels, and six SRTM DEM-based kernels) were employed to model the relationship between the input kernels and the target Landsat LSTs.

Landsat LSTs were derived from thermal infrared (TIR) data based on a single-channel (SC) algorithm (Jimenez-Munoz et al., 2008) (Table 2). Typically, the SC algorithm requires only one TIR band, resulting in a root mean squared error (RMSE) within 1.5 K compared to the ground truth (Jimenez-Munoz et al., 2014; Sobrino et al., 2004). To generate the downscaled LST (DLST), all 30 m input kernels were aggregated to 100 m and 120 m, which have the same resolution as the original Landsat thermal bands for 2004 and 2021.

### 3.3. Thermal environment analysis strategy

In this study, we developed an integrated approach to explore the urban thermal environment through urban renewal in Suwon by observing LULC changes during the study period using LCZ maps and their impact on surface temperature. In the temporal LCZ maps, only the built-types of LCZs were extracted to determine the intra-urban morphology transition impact on the thermal environment. To reduce the uncertainty caused by LCZ misclassification, we utilized probability maps obtained from the softmax function to filter out pixels with low probabilities. The threshold of the probability value was set when the  $OA_{urb}$  reached a target of 85%, which is required for satellite-based remote sensing classification studies (Anderson 1976; Li et al 2022; McNairn et al., 2009).

To quantitatively identify land transformation due to rapid urbanization in Suwon, a land-cover transformation matrix was generated. Matrix indicates the LCZ types and area conversion over the study period

(Equation (4)). This research involved the division of two distinct groups, namely the proposed filtering method and the original non-filtering method, for comparison.

$$LCZ_{ij} = \begin{bmatrix} LCZ_{11} & LCZ_{12} & \dots & LCZ_{1n} \\ LCZ_{21} & LCZ_{22} & \dots & LCZ_{2n} \\ \dots & \dots & \dots & \dots \\ LCZ_{n1} & LCZ_{n2} & \dots & LCZ_{nn} \end{bmatrix} \quad (4)$$

where  $n$  is the total number of LCZ classes in Suwon, and  $i$  and  $j$  indicate the LCZ types for 2004 and 2021, respectively. The values in each row represent the areas converted from LCZ type  $i$  to the other LCZ types. The values in all the columns reveal that the area transformed from other LCZ types to LCZ type  $j$ .

Although LST was derived from Landsat images captured during the same climate season and time of day to eliminate the adverse effects of different times, it may be subject to annual fluctuations in different years. Herein, to exclude annual LST variation and analyze the dynamic evolution of the thermal environment in different LCZs, the LST difference in the unchanged LCZ class between the LCZ map in 2004 and 2021 was assumed to be caused by interannual climate variation (Fig. 4). As for annual LST fluctuation, LST difference for the same LCZ class was normalized against all other LST differences using the following steps: 1) calculating LST difference between LCZ class in past and LCZ class in present, 2) evaluating LST difference for the same LCZ class during the study period (called basic change;  $\Delta$ ), and 3) subtracting the LST difference due to LCZ change from basic change (Equations (5), (6) and (7)). The LST normalization procedure was applied consistently to both the filtering and non-filtering approaches.

$$\overline{\Delta LST}_{ij} = LST_{i(2021)} - LST_{j(2004)} \quad (5)$$

$$\Delta LST_i = LST_{i(2021)} - LST_{i(2004)} \quad (6)$$

$$NLST = \overline{\Delta LST}_{ij} - \Delta LST_i \quad (7)$$

In summary, we formulated a three-step procedure to investigate the influence of dynamic LULC changes on the surface thermal behavior. First, LCZ and probability maps with 30 m resolution were delineated using a CNN-based LCZ model to identify LULC changes caused by urban expansion. Second, using the kernel-driven approach, 30 m resolution DLSTs were retrieved for 2004 and 2021. Third, using the aforementioned outputs, the LST variation due to built-type LCZs transformation was analyzed.

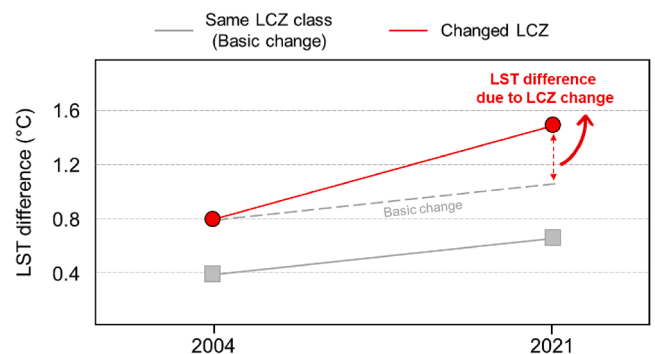


Fig. 4. The normalization method used in this study to mitigate annual LST fluctuation. Gray line represents average LST of the same LCZ class during the study period, gray dotted line means basic average LST change owing to annual variation and red line indicates average LST affected by LCZ class change, and Red dotted line designates average LST difference due to LCZ change.

## 4. Results

### 4.1. Temporal LCZ change analysis with accuracy assessment.

The Suwon LCZ maps for 2004 and 2021, along with noticeably changed locations (Site 1–3), are shown in Fig. 5; Table 4 illustrates the

proportion of LCZ types in Suwon from the LCZ maps of 2004 (Fig. 5a) and 2021 (Fig. 5b). From 2004 to 2021, the total built-type LCZ area increased, whereas the total natural-type LCZs area decreased. Among the built-type LCZs, the prevalence of low-rise urban forms, specifically LCZ3, LCZ6, and LCZ9, decreased, whereas that of mid-rise (LCZ2 and LCZ5) and high-rise forms (LCZ1 and LCZ4) increased, suggesting a

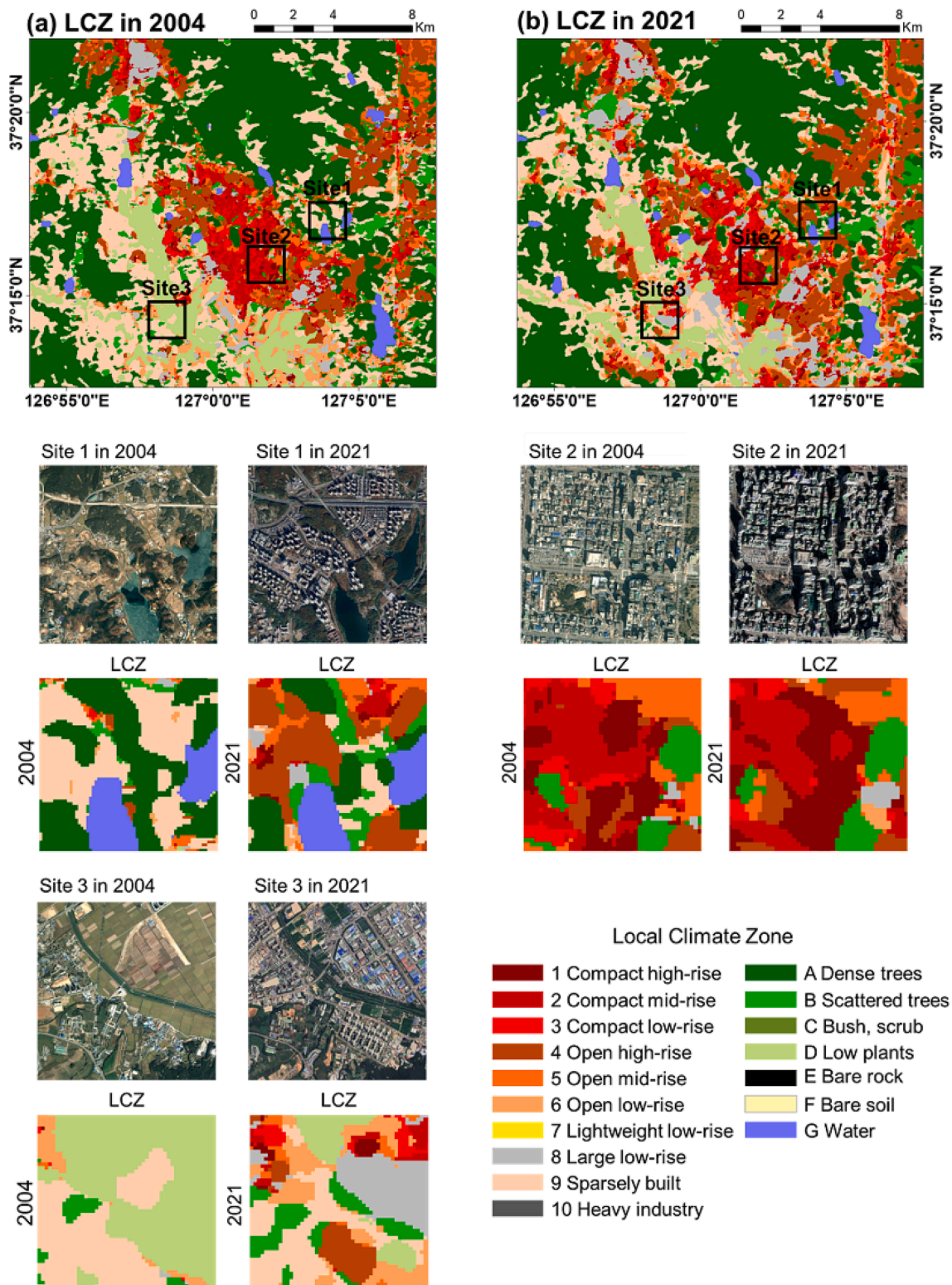


**Fig. 5.** Local Climate Zone (LCZ) maps in 2004 (a) and 2021 (b) with drastic changed locations (Sites 1–3). The black square delineates the areas shown in detail to compare land cover change. The images below bi-temporal LCZ maps indicate the specific site using Google Earth image (upper) and LCZs (below) over time.

**Table 4**

The proportion of the LCZ types in Suwon from 2004 to 2021 (%). The change indicates the proportion difference of LCZ types between 2004 and 2021 in Suwon.

Year	LCZ 1	LCZ 2	LCZ 3	LCZ 4	LCZ 5	LCZ 6	LCZ 8	LCZ 9	LCZ A	LCZ B	LCZ D	LCZ G
2004	1.50	3.45	3.38	9.04	4.12	6.03	3.41	19.81	34.55	5.90	7.03	1.80
2021	1.53	4.23	3.30	12.39	5.64	5.92	5.78	14.41	34.09	5.46	5.68	1.57
Change	0.03	0.78	-0.08	3.35	1.53	-0.11	2.37	-5.40	-0.46	-0.43	-1.34	-0.23

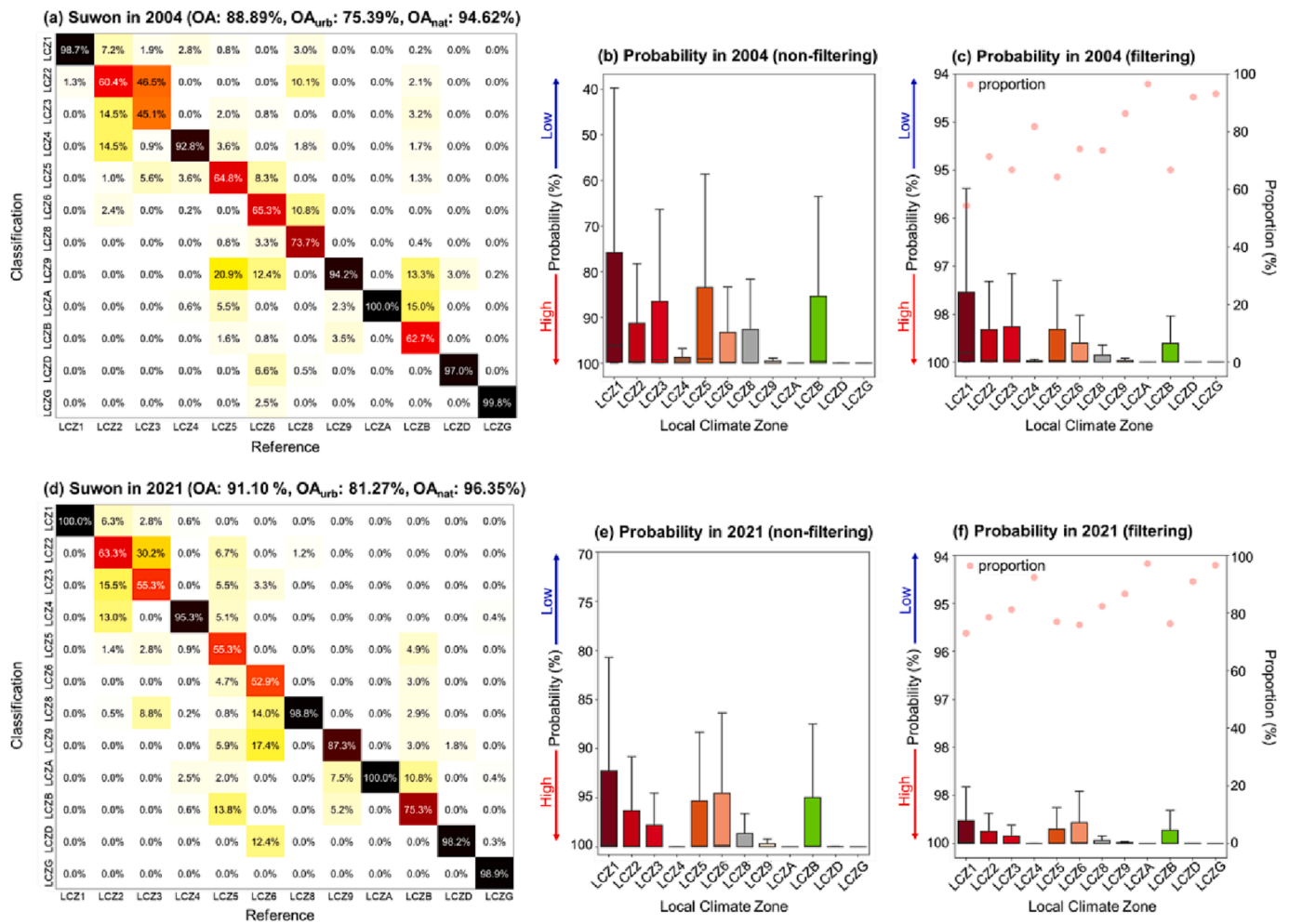
trend of vertical expansion. Notably, the urban development in LCZ4 (open high-rise) was the most extensive, with a 3.35% increase, followed by LCZ8 (large low-rise), with a 2.37% increase. A typical expansion at the urban fringe was observed at Sites 1 and 3 in Fig. 5, with conversions mainly from LCZ9 to LCZ4 and from LCZD to LCZ8, respectively. Interestingly, changes between built-up LCZs have also been identified (e.g., Site 2). In 2004, Site 2 was dominated by building forms LCZ2 or LCZ3; however, in 2021, a distribution of LCZ1 was found, indicating vertical growth. These results aligned with the LULC changes associated with population growth and urbanization in Suwon (<https://www.suwon.go.kr/stat/>).

Fig. 6 shows the classification accuracy for the bi-temporal LCZs with the Softmax probability for each LCZ class. The accuracy estimations for the LCZ maps of 2004 (Fig. 6a) and 2021 (Fig. 6d) were 88.89% and 91.10% for OA, 75.39% and 81.27% for OA<sub>urb</sub>, and 94.62% and 96.35% for OA<sub>nat</sub>. A disparity in the probability range (i.e., the y-axis) between Fig. 6b and Fig. 6e was observed, which was presumably attributable to

the sensor quality resulting from the technical methodology employed by Landsat 5 and Landsat 8 (Irons et al., 2012; Mishra et al., 2016). In both years, compared to natural-type LCZs (e.g., LCZA and D), relatively low mean and high variance of softmax probability values were shown in built-type LCZs (e.g., LCZs 1–3 and LCZs 5–8), where misclassification among them appeared due to heterogeneous urban surface structures (See also Supplementary Fig. S1). Only LCZs with a high level of confidence remained after applying the proposed filtering method, showing a proportion of 50% or more for each LCZ (Fig. 6c and f).

4.2. Evaluation and analysis for the downscaled LSTs

The average DLST for each year with detailed spatial patterns is given in Fig. 7. In the validation results of these maps (Supplementary Fig. S2), the coefficient of determination (R<sup>2</sup>) values were greater than 0.9 for all validation dates except for one (R<sup>2</sup> is 0.85 on March 31, 2004), whereas the RMSEs were below one degree Celsius for all validation



**Fig. 6.** LCZ classification accuracy assessment results based on confusion matrices of Suwon in 2004 (a) and 2021 (d); softmax-based probability distribution in 2004 (b) and 2021 (e) with non-filtering; and in 2004 (c) and 2021 (f) with filtering and proportion of remaining pixels. The probability threshold value was set at 94% for filtering.

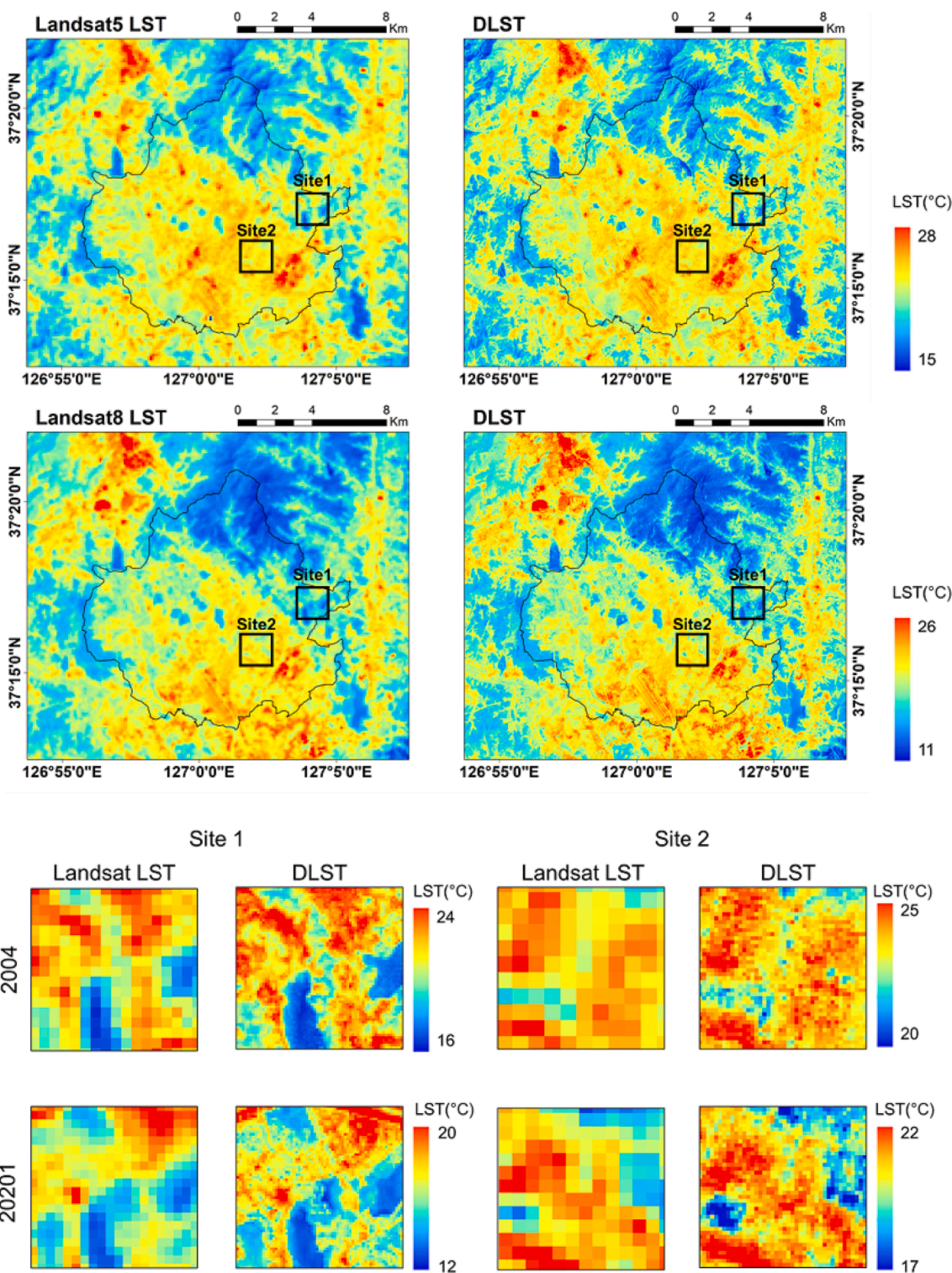


Fig. 7. Spatial distribution of average LST representing the study area in 2004 (upper) and 2021 (below). Each figure represents Landsat LST (left), and downscaled LST in this study (right). The enlarged images at Site 1 and Site 2 are shown. The upper images of each site describe the land cover characteristics in 2004 using Landsat LST (left) and downscaled LST (right) at the same location. The below images of each site depict 2021 in the same way.

dates. Compared with previous studies that used Landsat 8 to derive a 30 m LST for 32 cities worldwide (Dong et al., 2020), our validation results guarantee that DLSTs can describe convincing levels of surface temperature across a wide range of urban forms in Suwon.

The Landsat LSTs and DLSTs exhibited similar surface temperature distributions over the study period, with high LSTs over dense impervious surfaces. However, when examining Sites 1 and 2, the difference

between Landsat LSTs and DLSTs became evident when DLSTs provided a more detailed representation, capturing the sensitive variation in LST based on building form and characteristics. For example, the DLST effectively represents LCZ-type characteristics with affluent LST, not only at Site 1, where the built-type LCZs and natural-type LCZs coexist, but also at Site 2, where heterogeneous built-type LCZs are gathered (See also Fig. 5). This suggests that DLSTs can represent opulent thermals

over heterogeneous urban areas in addition to maintaining the general spatial pattern of Landsat LSTs.

The thermal behavior of each LCZ type is shown in Fig. 8. Among the 12 LCZ types in Suwon, LCZ8 and LCZ2 consistently maintained the highest LST values, whereas LCZG and LCZA had the lowest LST values without any differences in order (see their rankings in Fig. 8). However, it is worth noting that the built-up LCZs and LST characteristics in 2021 are more prominent than those in 2004, and some LST ranks have undergone changes. The spatial pattern of impervious surfaces affects the LST in various ways, and the LST tends to increase as the spatial concentration increases (Mathew et al., 2016; Zhang et al., 2009). The changes in the proportion of built-type LCZs observed during the bi-temporal period (Table 4) appear to be mirrored by the LCZ-LST characteristics of 2021.

### 4.3. LST variation by intra-urban transition

Fig. 9 illustrates the mean LST values according to changes in built-type LCZs using the proposed filtering method based on softmax probability maps (Fig. 9a) and the original non-filtering method (Fig. 9b). As shown in Fig. 5, sporadic bidirectional urban growth occurred in the study area, resulting in statistically significant LST variability with diverse magnitudes of most LCZ changes in both analyses (Fig. 9). Notably, in LCZ8, which recorded the highest temperature ranking in both periods, the observed changes showed the highest values in both maximum change (2.8 °C and 2.2 °C from LCZ9 to LCZ8, in the proposed method and original method, respectively) and minimum change

(-2.2 °C from LCZ8 to LCZ1 in the proposed method and -1.9 °C from LCZ8 to LCZ4 in the original method, respectively) among all the changes. Furthermore, distinct LST changes were observed in LCZ2, LCZ4, and LCZ8, which showed a substantial increase in the LCZ proportion compared to other built-type LCZs. In comparison to the LCZ compact types (LCZ 1–3) of the same height, changes toward the LCZ open types (LCZ 4–6) have a tendency toward negative temperature change, apparently due to the shape of open structures with surrounding vegetation, as reported in previous studies (Dian et al., 2020; Zhang et al., 2014; Zhu et al., 2019). In terms of LST variation due to vertical growth, the transition from LCZ low-rise types (LCZ3, LCZ6, and LCZ9) to LCZ high-rise types (LCZ1 and LCZ4) with the highest impervious surface fraction was smaller than the transition to LCZ mid-rise types (LCZ2 and LCZ5). This can be explained by previous research findings (Bechtel et al., 2019; Nassar et al., 2016; Perini and Magliocco, 2014), where high-rise buildings cast shadows that decrease the amount of solar radiation received by the surface compared with mid-rise buildings.

In the comparison between the proposed filtering method (Fig. 9a) and the original non-filtering method (Fig. 9b), the general trend of thermal variation according to built-type LCZs changes was consistently represented, regardless of whether filtering was applied. However, two distinct differences are observed between the two methods. First, it was shown that the proposed filtering method resulted in slightly higher LST variability in the range of - 0.4 °C to 0.6 °C compared to the original non-filtering method. The other difference is that we observed a reversal in the strength of the LST variability when filtering was applied in the

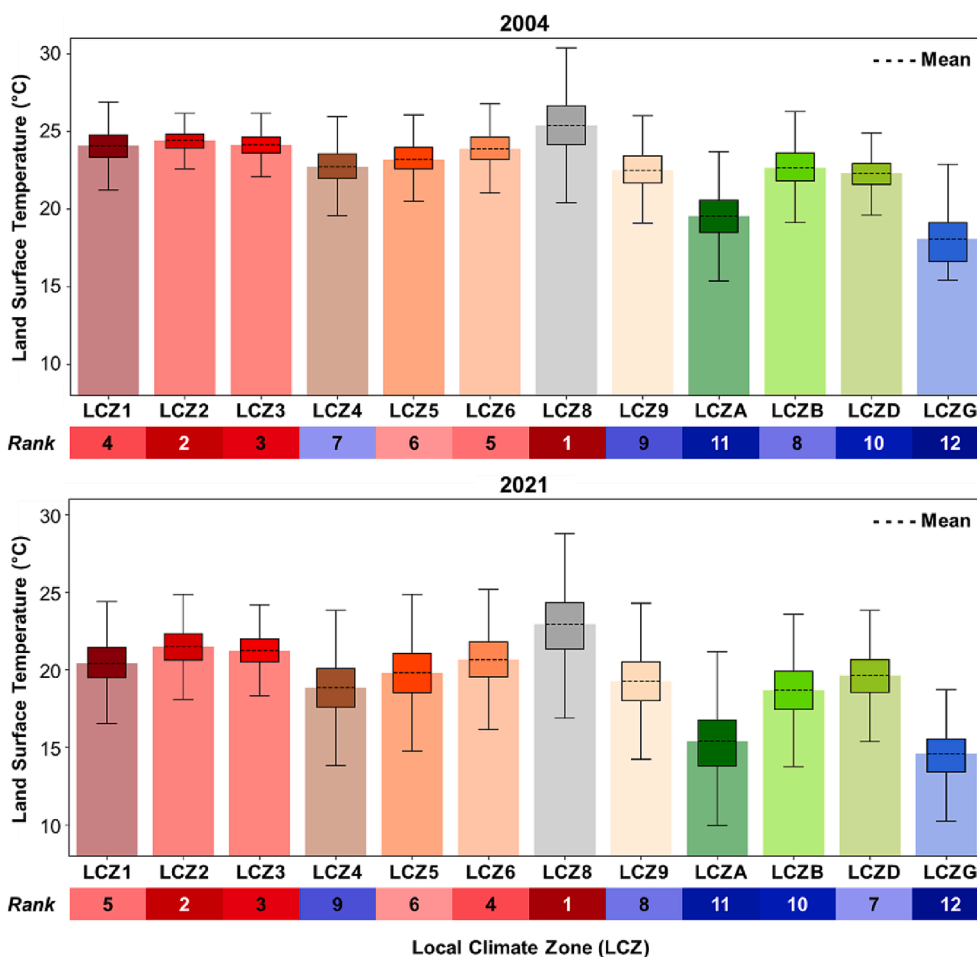
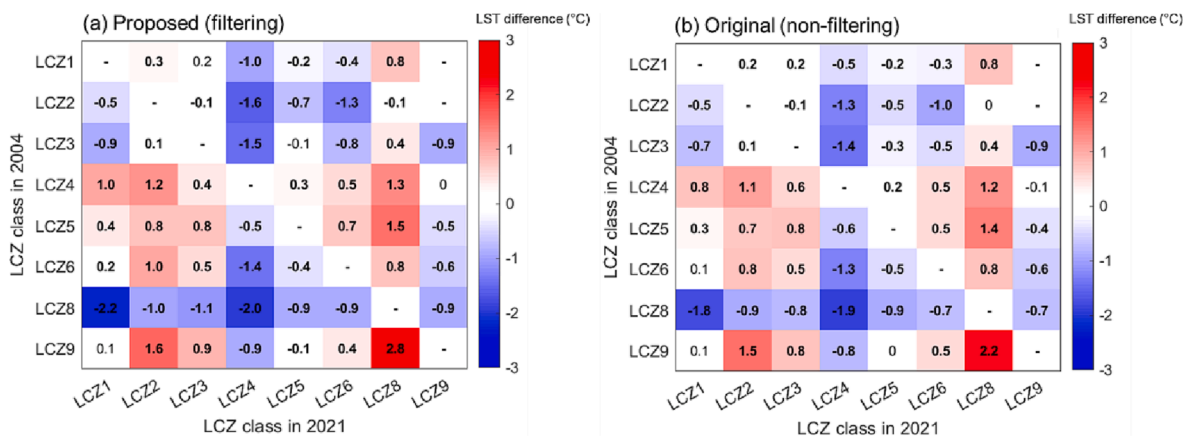


Fig. 8. Thermal variations of each LCZ type after filtering with a probability value of 0.94. The figure summarizes the maximum, minimum, median, average, and interquartile values of the LST characteristics of each LCZ class using boxplots and bar plots in 2004 and 2021. The number below LCZ type (x-axis) represents LST rank of each LCZ class.



**Fig. 9.** Thermal variations by built-type LCZ transformation with the proposed filtering method (a) and original non-filtering method (b). The values in the figure represent the mean LST difference between 2004 and 2021. Bold values denoting the mean LST difference are significant based on the Z-test at the 95% confidence level ( $p < 0.05$ ).

analysis. When transitioning from LCZ2 to LCZ4 and from LCZ3 to LCZ4, the proposed filtering method showed  $-1.6\text{ }^{\circ}\text{C}$  and  $-1.5\text{ }^{\circ}\text{C}$ , respectively, indicating a larger LST change in the former than in the latter. In contrast, the original method showed  $-1.3\text{ }^{\circ}\text{C}$  and  $-1.4\text{ }^{\circ}\text{C}$ , respectively, with larger values observed in the latter. This inversion was also observed in the transition from LCZ8 to LCZ2 and LCZ3. Compared with the original non-filtering method, the results of the proposed filtering method more clearly demonstrate the thermal behavior changes corresponding to the rank differences of each LCZ type (See Fig. 8), indicating contributions to the urban thermal environment analysis.

### 5. Discussion

With the advancement of remote sensing applications and the advent of LCZ classification schemes, diverse and in-depth urban climate research has been actively attempted. Many studies have utilized the LCZ scheme to analyze the impact of temporal LULC changes on urban thermal environments. However, this study differs from the previous studies in several ways. On the one hand, previous studies that observed temporal LULC changes using the LCZ mainly focused on horizontal expansion, transforming from natural areas to built-up areas (Han et al., 2022; Wang et al., 2019). On the other hand, we analyzed the thermal behavior based on intra-urban conversion. In this study, dynamic changes were observed in the temporal evolution of urban structures caused by urbanization, including significant structural changes within built-up areas. The results of our research align with those of a previous study that proposed urbanization as a consequence of bidirectional expansion (Bounoua et al., 2018). However, it should be noted that vertical growth within the built-up areas has not been comprehensively studied in previous research on urbanization dynamics over time. Our analysis of the urban thermal environment based on intra-urban transitions provides a paradigm shift in our understanding. This reflects practical urbanization, which has been overlooked as horizontal urbanization.

In contrast to previous studies that directly used LST products, this study generated 30 m LSTs using a kernel-driven downscaling method to analyze the thermal behavior due to dynamic transitions in heterogeneous urban areas. Although Landsat provides 30 m LST, its limitation lies in the cubic convolutional resampling method, which does not consider heat exchange processes in the urban environment (Xu et al., 2020). Typically, a fine resolution that can observe the widths of building blocks is required in urban climate research (Bechtel et al., 2012), and a high spatial resolution can improve the accuracy of urban thermal environment analyses (Stathopoulou and Cartalis, 2009). The generated DLST represents significant variations in surface temperature

in heterogeneous areas and shows high consistency with Landsat LST in spatial patterns, enabling the analysis of thermal behavior in urban areas according to dynamic transitions.

This study suggests a probabilistic filtering method to eliminate the uncertainty caused by low  $OA_{\text{urb}}$  in an LCZ-based urban thermal environmental analysis. Although the overall accuracy of LCZ mapping has significantly improved with the integration of AI technology and various data,  $OA_{\text{urb}}$  still fails to meet the accuracy required for thematic mapping in previous studies. Consequently, in some regions, a compromise in the accuracy is required (Wang et al., 2018; Zhao et al., 2020). The proposed probabilistic filtering approach can remedy the accuracy issue and was proven to be effective in reaching  $OA_{\text{urb}}$  with the required accuracy for analysis (Supplementary Fig. S3). However, because the proposed method has only been validated in one city, further research is needed, and the optimal probability threshold may vary depending on the study area.

Additionally, the proposed filtering method can be used as an alternative to reduce the uncertainty caused by misclassification. As shown in Fig. 9, the proposed filtering method showed a similar trend, but some differences were revealed when compared with the original non-filtering method. The rationale of the proposed filtering method can be explained as follows. First, the results in Fig. 8 are consistent with previous studies (Han et al., 2022; Wang et al., 2019) in those distinct differences in LST between built-type LCZs and natural-type LCZs were observed, with higher LST occurring in built-type LCZs and lower LST in natural-type LCZs, suggesting that there were no significant issues with the LCZ and LST results. However, as shown in Fig. 5, low probabilities were mainly distributed over built-type LCZs, and the required accuracy of  $OA_{\text{urb}}$  is confirmed in Supplementary Fig. S3 by applying the proposed filtering method. In other words, the original non-filtering analysis may contain uncertainty caused by misclassification. Based on these discussions, it can be inferred that the proposed filtering method, which captures more abundant thermal fluctuations in accordance with LCZ-LST attributes, has the potential to yield rational outcomes and enhance the sophisticated analysis of the urban thermal environment. Owing to the inherent LCZ classification errors caused by the absence of height data, the proposed filtering method could not entirely eliminate uncertainties in the analysis. Nevertheless, these improved distinctions may facilitate the advancement of sophisticated analyses of urban heat environments.

Owing to cloud contamination and noise in the satellite images used for the study area, the number of Landsat images obtained per year for LST retrieval remained limited. One possible approach to address this issue involves reconstructing LST under cloud cover (Fu et al., 2022; Zhu et al., 2022). However, uncertainty is associated with reconstructed LST data (Mo et al., 2021); hence, we did not apply reconstructed LST in this

study. Further investigation needs to be conducted to determine whether reconstructed LST can be applied in future studies of dynamic changes in urban thermal environmental patterns. Despite certain limitations, this study provides a baseline for a novel approach to urban climate in the era of artificial intelligence.

## 6. Conclusion

This study presents a new methodology for observing the impact of feasible LULC changes due to rapid urbanization on the urban thermal environment. To observe realistic bidirectional expansion at a detailed scale between 2004 and 2021, we generated 30 m resolution temporal LCZ maps and DLSTs. In addition, to reduce the analysis uncertainty caused by a low  $OA_{urb}$ , we proposed a novel analysis approach that extracts softmax-based probabilities from the LCZ classification model along with LCZ classes to remove areas with low classification confidence. Consequently, LST fluctuations due to intra-urban structural transition were observed, and the following conclusions were drawn. Noticeable variability in the LST was associated with changes in the proportion of LCZ types. In terms of vertical expansion, the transition to the compact mid-rise type showed the largest increase in LST, whereas the conversion to the open high-rise type resulted in a decrease in LST among the built-type LCZs. Applying the proposed filtering method facilitates the derivation of reasonable LST variability by eliminating regions with a low level of classification confidence. We expect that the proposed hybrid AI approach can be successfully applied to other global cities and will help us understand the urban thermal environment driven by dynamic land-cover change. In subsequent studies, it will be necessary to analyze the effects of urban thermal behavior according to seasonal characteristics and day-night variations in response to dynamic changes.

## Declaration of Competing Interest

The authors declare that they have no known competing financial interests or personal relationships that could have appeared to influence the work reported in this paper.

## Data availability

Data will be made available on request.

## Acknowledgements

This research was supported by the National Research Foundation of Korea under Grant NRF-2021R1A2C2C008561, by the Korea Meteorological Administration Research and Development Program under Grant KMIPA 2017-7010, and by Korea Institute of Marine Science & Technology Promotion (KIMST) funded by the Ministry of Oceans and Fisheries, Korea (RS-2023-00256330; RS-2023-00238486).

## Appendix A. Supplementary material

Supplementary data to this article can be found online at <https://doi.org/10.1016/j.jag.2023.103408>.

## References

Alhichri, H., Alswayed, A.S., Bazi, Y., Ammour, N., Alajlan, N.A., 2021. Classification of remote sensing images using EfficientNet-B3 CNN model with attention. *IEEE Access* 9, 14078–14094.

Alqurashi, A.F., Kumar, L., Sinha, P., 2016. Urban land cover change modelling using time-series satellite images: a case study of urban growth in five cities of Saudi Arabia. *Remote Sens. (Basel)* 8 (10), 838.

Anderson, J.R., 1976. A land use and land cover classification system for use with remote sensor data, Vol. 964. US Government Printing Office.

Bechtel, B., Zakšek, K., Hoshyaripour, G., 2012. Downscaling land surface temperature in an urban area: a case study for Hamburg, Germany. *Remote Sens.* 4 (10), 3184–3200.

Bechtel, B., Alexander, P., Böhner, J., Ching, J., Conrad, O., Feddema, J., Mills, G., See, L., Stewart, I., 2015. Mapping local climate zones for a worldwide database of the form and function of cities. *ISPRS Int. J. Geo Inf.* 4 (1), 199–219.

Bechtel, B., Demuzere, M., Mills, G., Zhan, W., Sismanidis, P., Small, C., Voogt, J., 2019. SUHI analysis using Local Climate Zones—A comparison of 50 cities. *Urban Clim.* 28, 100451.

Bhatta, B., 2009. Analysis of urban growth pattern using remote sensing and GIS: a case study of Kolkata, India. *Int. J. Remote Sens.* 30 (18), 4733–4746.

Bonafoni, S., 2016. Downscaling of Landsat and MODIS land surface temperature over the heterogeneous urban area of Milan. *IEEE J. Sel. Top. Appl. Earth Obs. Remote Sens.* 9 (5), 2019–2027.

Bouliila, W., Sellami, M., Driss, M., Al-Sarem, M., Safaei, M., Ghaleb, F.A., 2021. RS-DCNN: A novel distributed convolutional-neural-networks based-approach for big remote-sensing image classification. *Comput. Electron. Agric.* 182, 106014.

Bounoua, L., Nigro, J., Zhang, P., Thome, K., Lachir, A., 2018. Mapping urbanization in the United States from 2001 to 2011. *Appl. Geogr.* 90, 123–133.

Breiman, L., 2001. Random forests. *Machine Learn.* 45 (1), 5–32.

Cao, S., Cai, Y., Du, M., Weng, Q., Lu, L., 2022. Seasonal and diurnal surface urban heat islands in China: an investigation of driving factors with three-dimensional urban morphological parameters. *GISci. Remote Sensing* 59 (1), 1121–1142.

Chen, X., Jeong, S., Park, H., Kim, J., Park, C.-R., 2020. Urbanization has stronger impacts than regional climate change on wind stilling: a lesson from South Korea. *Environ. Res. Lett.* 15 (5), 054016.

Chen, Y.C., Lin, T.P., Shih, W.Y., 2017. March). Modeling the urban thermal environment distributions in Taipei Basin using Local Climate Zone (LCZ). In: *In 2017 Joint Urban Remote Sensing Event (JURSE)*. IEEE, pp. 1–4.

Cheval, S., Popa, A.-M., Şandric, I., Ioja, I.-C., 2020. Exploratory analysis of cooling effect of urban lakes on land surface temperature in Bucharest (Romania) using Landsat imagery. *Urban Clim.* 34, 100696.

Cho, D., Yoo, C., Im, J., Cha, D.H., 2020. Comparative assessment of various machine learning-based bias correction methods for numerical weather prediction model forecasts of extreme air temperatures in urban areas. *Earth and Space Sci.* 7 (4), e2019EA000740.

Demuzere, M., Bechtel, B., Mills, G., 2019. Global transferability of local climate zone models. *Urban Clim.* 27, 46–63.

Demuzere, M., Mihara, T., Redivo, C. P., Feddema, J., & Setton, E. 2020. Multi-temporal LCZ maps for Canadian functional urban areas.

Demuzere, M., Kittner, J., Martilli, A., Mills, G., Moede, C., Stewart, I.D., van Vliet, J., Bechtel, B., 2022. A global map of local climate zones to support earth system modelling and urban-scale environmental science. *Earth Syst. Sci. Data* 14 (8), 3835–3873.

Dian, C., Pongrácz, R., Dezsó, Z., Bartholy, J., 2020. Annual and monthly analysis of surface urban heat island intensity with respect to the local climate zones in Budapest. *Urban Clim.* 31, 100573.

Dong, P., Gao, L., Zhan, W., Liu, Z., Li, J., Lai, J., Li, H., Huang, F., Tamang, S.K., Zhao, L., 2020. Global comparison of diverse scaling factors and regression models for downscaling Landsat-8 thermal data. *ISPRS J. Photogramm. Remote Sens.* 169, 44–56.

Dugord, P.A., Lauf, S., Schuster, C., Kleinschmit, B., 2014. Land use patterns, temperature distribution, and potential heat stress risk—the case study Berlin, Germany. *Comput. Environ. Urban Syst.* 48, 86–98.

Fan, P.Y., Chun, K.P., Mijic, A., Mah, D.-Y., He, Q., Choi, B., Lam, C.K.C., Yetemen, O., 2022. Spatially-heterogeneous impacts of surface characteristics on urban thermal environment, a case of the Guangdong-Hong Kong-Macau Greater Bay Area. *Urban Clim.* 41, 101034.

Feyisa, G.L., Meilby, H., Jenerette, G.D., Pauliet, S., 2016. Locally optimized separability enhancement indices for urban land cover mapping: exploring thermal environmental consequences of rapid urbanization in Addis Ababa, Ethiopia. *Remote Sens. Environ.* 175, 14–31.

Fu, H., Shao, Z., Fu, P., Huang, X., Cheng, T., Fan, Y., 2022. Combining ATC and 3D-CNN for reconstructing spatially and temporally continuous land surface temperature. *Int. J. Appl. Earth Obs. Geoinf.* 108, 102733.

Fu, P., Weng, Q., 2016. A time series analysis of urbanization induced land use and land cover change and its impact on land surface temperature with Landsat imagery. *Remote Sens. Environ.* 175, 205–214.

Geletić, J., Lehnert, M., Savić, S., Milošević, D., 2019. Inter-/intra-zonal seasonal variability of the surface urban heat island based on local climate zones in three central European cities. *Build. Environ.* 156, 21–32.

Guidici, D., Clark, M.L., 2017. One-Dimensional convolutional neural network land-cover classification of multi-seasonal hyperspectral imagery in the San Francisco Bay Area, California. *Remote Sens.* 9 (6), 629.

Guo, Y., Ren, Z., Dong, Y., Hu, N., Wang, C., Zhang, P., Jia, G., He, X., 2022. Strengthening of surface urban heat island effect driven primarily by urban size under rapid urbanization: national evidence from China. *GISci. Remote Sens.* 59 (1), 2127–2143.

Han, B., Luo, Z., Liu, Y., Zhang, T., Yang, L., 2022. Using Local Climate Zones to investigate Spatio-temporal evolution of thermal environment at the urban regional level: a case study in Xi'an, China. *Sustainable Cities and Soc.* 76, 103495.

Harlan, S.L., Brazel, A.J., Prasad, L., Stefanov, W.L., Larsen, L., 2006. Neighborhood microclimates and vulnerability to heat stress. *Soc. Sci. Med.* 63 (11), 2847–2863.

Ho, H.C., Knudby, A., Sirovyak, P., Xu, Y., Hodul, M., Henderson, S.B., 2014. Mapping maximum urban air temperature on hot summer days. *Remote Sens. Environ.* 154, 38–45.

Hutengs, C., Vohland, M., 2016. Downscaling land surface temperatures at regional scales with random forest regression. *Remote Sens. Environ.* 178, 127–141.

- Irons, J.R., Dwyer, J.L., Barsi, J.A., 2012. The next Landsat satellite: the Landsat data continuity mission. *Remote Sens. Environ.* 122, 11–21.
- Jiménez-Muñoz, J.C., Cristobal, J., Sobrino, J.A., Soria, G., Ninyerola, M., Pons, X., Pons, X., 2009. Revision of the single-channel algorithm for land surface temperature retrieval from Landsat thermal-infrared data. *IEEE Trans. Geosci. Remote Sens.* 47 (1), 339–349.
- Jiménez-Muñoz, J.C., Sobrino, J.A., Skoković, D., Mattar, C., Cristobal, J., 2014. Land surface temperature retrieval methods from Landsat-8 thermal infrared sensor data. *IEEE Geosci. Remote Sens. Lett.* 11 (10), 1840–1843.
- Kattenborn, T., Leitloff, J., Schiefer, F., Hinz, S., 2021. Review on Convolutional Neural Networks (CNN) in vegetation remote sensing. *ISPRS J. Photogramm. Remote Sens.* 173, 24–49.
- Kim, M., Lee, J., Han, D., Shin, M., Im, J., Lee, J., Quackenbush, L.J., Gu, Z., 2018. Convolutional neural network-based land cover classification using 2-D spectral reflectance curve graphs with multitemporal satellite imagery. *IEEE J. Sel. Top. Appl. Earth Obs. Remote Sens.* 11 (12), 4604–4617.
- Kotharkar, R., Bagade, A., 2018. Local Climate Zone classification for Indian cities: a case study of Nagpur. *Urban Clim.* 24, 369–392.
- Lee, B.S., Chun, S.E., Kim, S.Y., 2007. The effects of regional characteristics on population growth in Korean cities, counties and wards. *J. Asian Econ.* 18 (3), 490–508.
- Lee, Y., Lee, S., Im, J., & Yoo, C. (2021). Analysis of surface urban heat island and land surface temperature using deep learning based local climate zone classification: A case study of suwon and daegu, korea.
- Li, Z.-L., Tang, B.-H., Wu, H., Ren, H., Yan, G., Wan, Z., Trigo, I.F., Sobrino, J.A., 2013. Satellite-derived land surface temperature: current status and perspectives. *Remote Sens. Environ.* 131, 14–37.
- Li, D., Wang, S., He, Q., Yang, Y., 2022. Cost-effective land cover classification for remote sensing images. *J. Cloud Comput.* 11 (1), 1–12.
- Liou, Y.-A., Nguyen, K.-A., Ho, L.-T., 2021. Altering urban greenspace patterns and heat stress risk in Hanoi city during Master Plan 2030 implementation. *Land Use Policy* 105, 105405.
- Liu, L., Zhang, Y., 2011. Urban heat island analysis using the Landsat TM data and ASTER data: a case study in Hong Kong. *Remote Sens. (Basel)* 3 (7), 1535–1552.
- Ma, L., Zhu, X., Qiu, C., Blaschke, T., Li, M., 2021. Advances of local climate zone mapping and its practice using object-based image analysis. *Atmos.* 12 (9), 1146.
- Masolele, R.N., De Sy, V., Herold, M., Marcos, D., Verbesselt, J., Gieseke, F., Mullissa, A. G., Martius, C., 2021. Spatial and temporal deep learning methods for deriving land-use following deforestation: a pan-tropical case study using Landsat time series. *Remote Sens. Environ.* 264, 112600.
- Mathew, A., Khandelwal, S., Kaul, N., 2016. Spatial and temporal variations of urban heat island effect and the effect of percentage impervious surface area and elevation on land surface temperature: Study of Chandigarh city, India. *Sustain. Cities Soc.* 26, 264–277.
- McNairn, H., Champagne, C., Shang, J., Holmstrom, D., Reichert, G., 2009. Integration of optical and Synthetic Aperture Radar (SAR) imagery for delivering operational annual crop inventories. *ISPRS J. Photogramm. Remote Sens.* 64 (5), 434–449.
- Middel, A., Häb, K., Brazel, A.J., Martin, C.A., Guhathakurta, S., 2014. Impact of urban form and design on mid-afternoon microclimate in Phoenix Local Climate Zones. *Landscape Urban Plan.* 122, 16–28.
- Mishra, N., Helder, D., Barsi, J., Markham, B., 2016. Continuous calibration improvement in solar reflective bands: landsat 5 through Landsat 8. *Remote Sens. Environ.* 185, 7–15.
- Mo, Y., Xu, Y., Chen, H., Zhu, S., 2021. A review of reconstructing remotely sensed land surface temperature under cloudy conditions. *Remote Sens. (Basel)* 13 (14), 2838.
- Mohammad, P., Goswami, A., 2021. Quantifying diurnal and seasonal variation of surface urban heat island intensity and its associated determinants across different climatic zones over Indian cities. *GIScience & Remote Sensing* 58 (7), 955–981.
- Nassar, A.K., Blackburn, G.A., Whyatt, J.D., 2016. Dynamics and controls of urban heat sink and island phenomena in a desert city: development of a local climate zone scheme using remotely-sensed inputs. *Int. J. Appl. Earth Obs. Geoinf.* 51, 76–90.
- Oke, T. R. 1995. The heat island of the urban boundary layer: characteristics, causes and effects. *Wind climate in cities*, 81–107.
- Peng, W., Yuan, X., Gao, W., Wang, R., Chen, W., 2021. Assessment of urban cooling effect based on downscaled land surface temperature: a case study for Fukuoka. *Japan. Urban Climate* 36, 100790.
- Perini, K., Magliocco, A., 2014. Effects of vegetation, urban density, building height, and atmospheric conditions on local temperatures and thermal comfort. *Urban For. Urban Green.* 13 (3), 495–506.
- Qiu, C., Tong, X., Schmitt, M., Bechtel, B., Zhu, X.X., 2020. Multilevel feature fusion-based CNN for local climate zone classification from sentinel-2 images: benchmark results on the So2Sat LC242 dataset. *IEEE J. Sel. Top. Appl. Earth Obs. Remote Sens.* 13, 2793–2806.
- Reddy, K. N. 1996. *Urban redevelopment: a study of high-rise buildings*. Concept publishing company.
- Rosentreter, J., Hagenseker, R., Waske, B., 2020. Towards large-scale mapping of local climate zones using multitemporal Sentinel 2 data and convolutional neural networks. *Remote Sens. Environ.* 237, 111472.
- Rwanga, S.S., Ndambuki, J.M., 2017. Accuracy assessment of land use/land cover classification using remote sensing and GIS. *Int. J. Geosci.* 08 (04), 611–622.
- Sera, F., Armstrong, B., Tobias, A., Vicedo-Cabrera, A.M., Åström, C., Bell, M.L., Chen, B.-Y., de Sousa Zanotti Stagliorio Coelho, M., Matus Correa, P., Cruz, J.C., Dang, T.N., Hurtado-Diaz, M., Do Van, D., Forsberg, B., Guo, Y.L., Guo, Y., Hashizume, M., Honda, Y., Iñiguez, C., Jaakkola, J.J.K., Kan, H., Kim, H.o., Lavigne, E., Michelozzi, P., Ortega, N.V., Osorio, S., Pascal, M., Ragetti, M.S., Rytli, N.R.I., Saldiva, P.H.N., Schwartz, J., Scortichini, M., Seposo, X., Tong, S., Zanobetti, A., Gasparrini, A., 2019. How urban characteristics affect vulnerability to heat and cold: a multi-country analysis. *Int. J. Epidemiol.* 48 (4), 1101–1112.
- Sobrino, J.A., Jiménez-Muñoz, J.C., Paolini, L., 2004. Land surface temperature retrieval from LANDSAT TM 5. *Remote Sens. Environ.* 90 (4), 434–440.
- Stathopoulou, M., Cartalis, C., 2009. Downscaling AVHRR land surface temperatures for improved surface urban heat island intensity estimation. *Remote Sens. Environ.* 113 (12), 2592–2605.
- Stewart, I.D., Oke, T.R., 2012. Local climate zones for urban temperature studies. *Bull. Am. Meteorol. Soc.* 93 (12), 1879–1900.
- Tomlinson, C.J., Chapman, L., Thornes, J.E., Baker, C., 2011. Remote sensing land surface temperature for meteorology and climatology: a review. *Meteorol. Appl.* 18 (3), 296–306.
- Trigo, I.F., Monteiro, I.T., Olesen, F., Kabsch, E., 2008. An assessment of remotely sensed land surface temperature. *J. Geophys. Res. Atmos.* 113 (D17).
- Unger, J., Lelovics, E., Gál, T., 2014. Local Climate Zone mapping using GIS methods in Szeged. *Hungarian Geographical Bulletin* 63 (1), 29–41.
- Verburg, P.H., Neumann, K., Nol, L., 2011. Challenges in using land use and land cover data for global change studies. *Glob. Chang. Biol.* 17 (2), 974–989.
- Verdonck, M.-L., Okujeni, A., van der Linden, S., Demuzere, M., De Wulf, R., Van Coillie, F., 2017. Influence of neighbourhood information on 'Local Climate Zone' mapping in heterogeneous cities. *Int. J. Appl. Earth Obs. Geoinf.* 62, 102–113.
- Wang, R., Cai, M., Ren, C., Bechtel, B., Xu, Y., Ng, E., 2019. Detecting multi-temporal land cover change and land surface temperature in Pearl River Delta by adopting local climate zone. *Urban Clim.* 28, 100455.
- Wang, C., Middel, A., Myint, S.W., Kaplan, S., Brazel, A.J., Lukaszczuk, J., 2018. Assessing local climate zones in arid cities: the case of Phoenix, Arizona and Las Vegas, Nevada. *ISPRS J. Photogramm. Remote Sens.* 141, 59–71.
- Weng, Q., Lu, D., 2008. A sub-pixel analysis of urbanization effect on land surface temperature and its interplay with impervious surface and vegetation coverage in Indianapolis, United States. *Int. J. Appl. Earth Obs. Geoinf.* 10 (1), 68–83.
- Xia, H., Chen, Y., Song, C., Li, J., Quan, J., Zhou, G., 2022. Analysis of surface urban heat islands based on local climate zones via spatiotemporally enhanced land surface temperature. *Remote Sens. Environ.* 273, 112972.
- Xian, G., Shi, H., Auch, R., Gallo, K., Zhou, Q., Wu, Z., Kolian, M., 2021. The effects of urban land cover dynamics on urban heat island intensity and temporal trends. *GIScience & Remote Sensing* 58 (4), 501–515.
- Xu, J., Zhang, F., Jiang, H., Hu, H., Zhong, K., Jing, W., Yang, J.i., Jia, B., 2020. Downscaling ASTER land surface temperature over urban areas with machine learning-based area-to-point regression Kriging. *Remote Sens. (Basel)* 12 (7), 1082.
- Yang, J., Wang, Y., Xiu, C., Xiao, X., Xia, J., Jin, C., 2020. Optimizing local climate zones to mitigate urban heat island effect in human settlements. *J. Clean. Prod.* 275, 123767.
- Yoo, C., Han, D., Im, J., Bechtel, B., 2019. Comparison between convolutional neural networks and random forest for local climate zone classification in mega urban areas using Landsat images. *ISPRS J. Photogramm. Remote Sens.* 157, 155–170.
- Yoo, C., Im, J., Park, S., Cho, D., 2020. Spatial downscaling of MODIS land surface temperature: Recent research trends, challenges, and future directions. *Korean J. Remote Sensing* 36 (4), 609–626.
- Yoo, C., Im, J., Cho, D., Lee, Y., Bae, D., Sismanidis, P., 2022. Downscaling MODIS nighttime land surface temperatures in urban areas using ASTER thermal data through local linear forest. *Int. J. Appl. Earth Obs. Geoinf.* 110, 102827.
- Zawadzka, J., Corstanje, R., Harris, J., Truckell, L., 2020. Downscaling Landsat-8 land surface temperature maps in diverse urban landscapes using multivariate adaptive regression splines and very high resolution auxiliary data. *Int. J. Digital Earth* 13 (8), 899–914.
- Zhang, Y., Odeh, I.O., Han, C., 2009. Bi-temporal characterization of land surface temperature in relation to impervious surface area, NDVI and NDBI, using a sub-pixel image analysis. *Int. J. Appl. Earth Obs. Geoinf.* 11 (4), 256–264.
- Zhang, H., Qi, Z.F., Ye, X.Y., Cai, Y.B., Ma, W.C., Chen, M.N., 2013. Analysis of land use/land cover change, population shift, and their effects on spatiotemporal patterns of urban heat islands in metropolitan Shanghai, China. *Appl. Geogr.* 44, 121–133.
- Zhang, B., Xie, G.-d., Gao, J.-x., Yang, Y., 2014. The cooling effect of urban green spaces as a contribution to energy-saving and emission-reduction: a case study in Beijing, China. *Build. Environ.* 76, 37–43.
- Zhao, C., Jensen, J.L., Weng, Q., Currit, N., Weaver, R., 2020. Use of local climate zones to investigate surface urban heat islands in Texas. *GIScience & Remote Sensing* 57 (8), 1083–1101.
- Zhao, C., Weng, Q., Wang, Y., Hu, Z., Wu, C., 2022. Use of local climate zones to assess the spatiotemporal variations of urban vegetation phenology in Austin, Texas, USA. *GIScience & Remote Sensing* 59 (1), 393–409.
- Zhu, X., Duan, S.-B., Li, Z.-L., Wu, P., Wu, H., Zhao, W., Qian, Y., 2022. Reconstruction of land surface temperature under cloudy conditions from Landsat 8 data using annual temperature cycle model. *Remote Sens. Environ.* 281, 113261.
- Zhu, X. X., Hu, J., Qiu, C., Shi, Y., Kang, J., Mou, L., ... & Wang, Y. 2019. So2Sat LC242: A benchmark dataset for global local climate zones classification. *arXiv preprint arXiv:1912.12171*.